Acta Pharmaceutica Sinica B 2023;13(11):4591–4606

Chinese Pharmaceutical Association
Institute of Materia Medica, Chinese Academy of Medical Sciences

Acta Pharmaceutica Sinica B

www.elsevier.com/locate/apsb
www.sciencedirect.com

ORIGINAL ARTICLE

Engineering cannabidiol synergistic carbon monoxide nanocomplexes to enhance cancer therapy *via* excessive autophagy

Chang Xiao[a], Yue Sun[a,b], Jialong Fan[a], William Nguyen[d], Simin Chen[a], Ying Long[a], Wei Chen[d,*], Aiguo Zhu[c,*], Bin Liu[a,*]

[a]*College of Biology, Hunan University, Changsha 410082, China*
[b]*General Hospital of Ningxia Medical University, School of Public Health and Management, Ningxia Medical University, Yinchuan 750004, China*
[c]*Institute of Bast Fiber Crops, Chinese Academy of Agricultural Sciences, Changsha 410205, China*
[d]*Department of Physics, the University of Texas at Arlington, Arlington, TX 76019, USA*

Received 3 February 2023; received in revised form 27 April 2023; accepted 30 April 2023

KEY WORDS

Carbon monoxide therapy;
Cannabidiol;
Reactive oxygen species;
Excessive autophagy;
Autophagic flux;
Autolysosome degradation;
Metastases;
Triple-negative breast cancer

Abstract Although carbon monoxide (CO)-based treatments have demonstrated the high cancer efficacy by promoting mitochondrial damage and core-region penetrating ability, the efficiency was often compromised by protective autophagy (mitophagy). Herein, cannabidiol (CBD) is integrated into biomimetic carbon monoxide nanocomplexes (HMPOC@M) to address this issue by inducing excessive autophagy. The biomimetic membrane not only prevents premature drugs leakage, but also prolongs blood circulation for tumor enrichment. After entering the acidic tumor microenvironment, carbon monoxide (CO) donors are stimulated by hydrogen oxide (H_2O_2) to disintegrate into CO and Mn^{2+}. The comprehensive effect of CO/Mn^{2+} and CBD can induce ROS-mediated cell apoptosis. In addition, HMPOC@M-mediated excessive autophagy can promote cancer cell death by increasing autophagic flux *via* class III PI3K/BECN1 complex activation and blocking autolysosome degradation *via* LAMP1 downregulation. Furthermore, *in vivo* experiments showed that HMPOC@M+ laser strongly inhibited tumor growth and attenuated liver and lung metastases by downregulating VEGF and MMP9 proteins. This strategy may highlight the pro-death role of excessive autophagy in TNBC treatment, providing a novel yet versatile avenue to enhance the efficacy of CO treatments. Importantly, this work also indicated the applicability of CBD for triple-negative breast cancer (TNBC) therapy through excessive autophagy.

*Corresponding authors.
E-mail addresses: weichen@uta.edu (Wei Chen), zhuaiguo@caas.cn (Aiguo Zhu), binliu2001@hotmail.com (Bin Liu).
Peer review under responsibility of Chinese Pharmaceutical Association and Institute of Materia Medica, Chinese Academy of Medical Sciences.

https://doi.org/10.1016/j.apsb.2023.05.019

1. Introduction

As an endogenousgaseous molecule, CO showed various biological functions including anti-inflammatory[1], anti-proliferative[2], pro-apoptotic properties[3], and so on. Meanwhile, this kind of gas can interfere with cytochrome *c* oxidase of mitochondrial electron transport chain to accelerate cellular respiration and ATP depletion[4,5]. Such metabolic processes lead to reactive oxygen species (ROS) production, thereby promoting cell apoptosis. Moreover, CO can easily traverse across diverse tumor interstitium and biological membranes[6]. Based on these encouraging properties, CO-based therapy has become an emerging modality for the noninvasive treatment of tumors[7]. For example, Huang et al.[8] prepared a multi-enzyme active CO nanoplatform to promote cancer therapy through mitochondrial energy depletion.

Given the ROS-induced mitochondrial damage, the subsequent energy depletion could predispose tumor cells into autophagy[9], a classical cellular defense mechanism by degrading damaged organelles and potentially toxic cytoplasmic material in cancers[10,11]. For example, CO induced mitochondrial biogenesis and protective autophagy through moderating ER stimulation as a tumor cell survival mechanism[12]. To avoid the protective effect of autophagy on tumor, several inhibitors, such as chloroquine (CQ)[13], 3-methyladenine (3-MA)[14] and bafilomycin A1 (Baf-A1), have been used to inhibit autophagy to improve cancer therapy, but the multiple clinical trials on cancer patients have been disappointing[15,16]. Especially in TNBC, ER-negative patients exhibited downregulation of BECN1, a key autophagic protein and tumor suppressor[17], and poorer survival to promote tumor progression[18,19,17]. Moreover, autophagy inhibition in TNBC cells induced the secretion of macrophage migration inhibitory factors[20]. Thus, based on the threshold effect of autophagy in the balance of cell death/survival[11,21], many studies have highlighted the beneficial role of autophagy activation in cancer therapy[18,22]. Especially, many drugs also cause irreversible destruction of cell contents through sustained or even excessive autophagy[22], which ultimately leads to cell death. Thus, inducing excessive autophagy by adopting optimal strategies can co-operate with CO-based strategy to improve the efficacy of cancer therapy.

Cannabidiol (CBD) is a main active ingredient extracted from *Cannabis sativa*[23]. Unlike the common phytocannabinoid tetrahydrocannabinol (THC), without psychogenic side effects, CBD is a promising chemotherapeutic drug candidate for various diseases therapy[24]. In primary reports, CBD can induce autophagy and ROS accumulation in breast cancer cells[25], but not for normal mammary gland cells[26]. Recently, CBD was used for glioblastoma therapy by activating Jun N-terminal kinase 1/2 (JNK1/2) pathway[27]. JNK activation drives the phosphorylation of BCL-2, which disrupts the competitive interaction between BECN1 and BCL-2[28], leading to autophagy-mediated cell death. Interestingly, the downregulation of CBD on lysosomal-associated membrane protein 1 (LAMP1) maybe contribute to the blockage of autophagic degradation[29]. Thus, we proposed that CBD could be a potential candidate for enhancing the efficacy of chemo/CO therapy against triple-negative breast cancer (TNBC) through excessive autophagy.

To test the possibility of this hypothesis, a biomimetic CBD synergistic CO nanocomplex (HMPB@MnCO@CBD@M, abbreviated as HMPOC@M) was developed for TNBC therapy (Scheme 1). In this nanocomplex, MnCO (CO precursor) was loaded into the cavity of prussian blue nanoparticles (PB NPs) and CBD molecules were stacked on the surface of PB NPs with the assistance of amphiphilic PPG-13-decyltetradeceth-24 (GS-01). Finally, hybrid membranes (M) prepared from RBC and 4T1 cells were adopted to endow targeting ability and improve the biocompatibility of this nanocomplex. After internalizing into tumor cells, MnCO can efficiently react with endogenous H_2O_2 to produce CO and Mn^{2+} at weak acidic environment. The CO can interfere with mitochondrial electron respiratory chain and Mn^{2+} can induce ·OH generation through Fenton reaction to kill tumor cells. In addition, NIR irradiation can accelerate CBD detachment from this nanocomplex. The released CBD can disrupt the antioxidant defense system by inhibiting NRF2 expression, thus promoting ROS production to kill tumor cells. Moreover, HMPOC@M can enhance the accumulation of autophagosomes by regulating ROS/JNK/BECN1 pathway, and CBD can disrupt the formation of autolysosomes by downregulating LAMP1, finally resulting in the occurrence of excessive autophagy for cell death. Collectively, the combined chemo/CO strategy can achieve high efficacy in TNBC therapy by inducing high ROS level and excessive autophagy. This strategy provided a new horizon for the application of CBD on clinical TNBC therapy.

2. Materials and methods

2.1. Materials and reagents

$K3[Fe(CN)6]\cdot 3H_2O$ and Poly (*N*-vinylpyrrolidone) (PVP) were obtained from Sinopharm Chemical Reagent Co., Ltd. (China). Cannabidiol (CBD) was presented by Institute of Bast Fiber Crops, Chinese Academy of Agricultural Sciences (Changsha, China). PPG-13-DECYLTETRADECETH-24 (GS-01) was purchased from Nippon Oil Corporation (Shanghai, China). MnCO was obtained from Sigma−Aldrich (USA). DAPI, DiO, DiI, and DiD, Membrane protein extraction kit, JC-1 kit, ATP assay kit, LysoTracker, Aminophenyl fluorescein and Acridine Orange were purchased from Beyotime (Shanghai, China). Hoechst 33342, ROS kit, TUNEL detection kit and Calcein AM/Propidium Iodide (PI) kit were purchased from Yeasen biotech Co., Ltd. (Shanghai, China). 3-Methyladenine (3-MA), chloroquine (CQ) and rapamycin (RAPA) were bought from MedChemExpress (Shanghai, China). Other chemicals and reagents were analytical grade. Antibodies including anti-BECN1, anti-SQSTM1, anti-NRF2, anti-JNK, anti-PARKIN, anti-AMPK, anti-p-AMPK, anti-MMP-9, anti-CD44 and anti-GAPDH were purchased from Proteintech (IL, USA). anti-VEGF and anti-PINK1 were obtained from Beyotime (Shanghai, China). anti-CD47 and anti-ACTIN were purchased

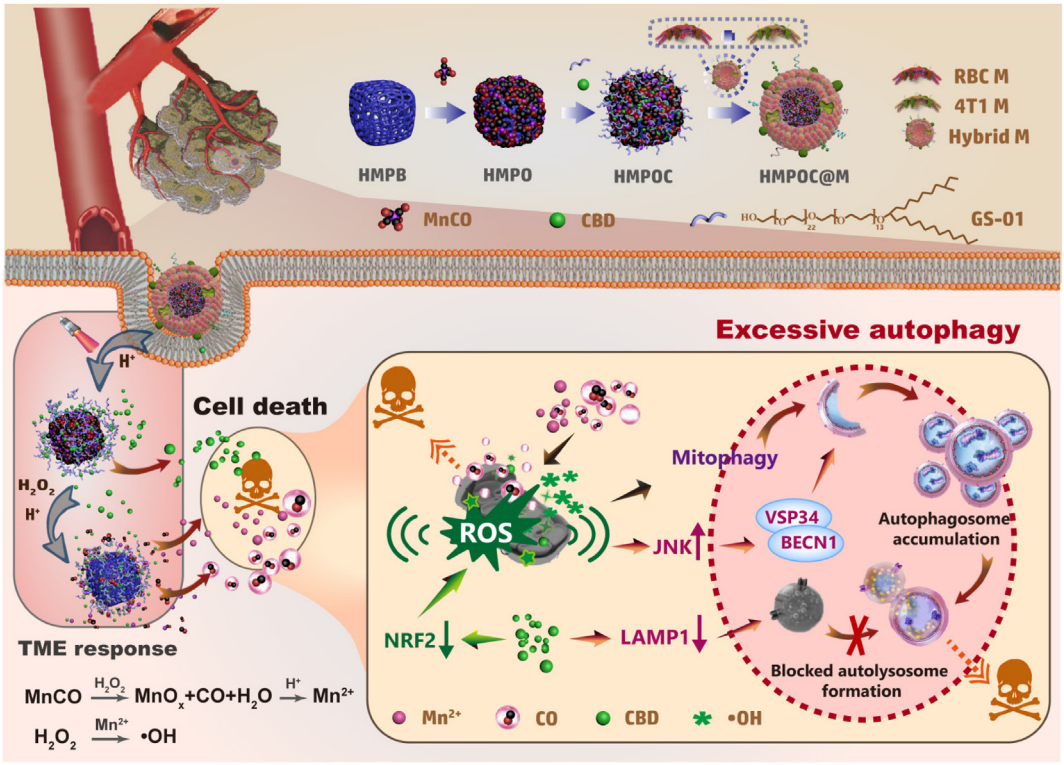

Scheme 1 Schematic illustration of cannabidiol synergistic carbon monoxide nanocomplexes (HMPOC@M) to enhance cancer therapy *via* excessive autophagy.

from Bioss (Beijing, China). anti-LC3A/B and anti-LAMP1 were obtained from Cell Signaling Technology.

2.2. *Synthesis of CO fluorescence probe (FL-CO-1)*

FL-CO-1 was synthesized according to the previous report[30], and its structure was shown in Supporting Information Fig. S6. ^{1}H NMR (600 MHz, DMSO-d_6) δ = 8.08 (dt, J = 7.7, 1.0, 1H), 7.84 (td, J = 7.5, 1.2, 1H), 7.78 (td, J = 7.5, 1.0, 1H), 7.47−7.36 (m, 3H), 7.08 (dd, J = 8.7, 2.4, 2H), 6.93 (d, J = 8.7, 2H), 6.01 (ddt, J = 17.3, 10.5, 5.6, 2H), 5.43 (dq, J = 17.3, 1.6, 2H), 5.32 (dq, J = 10.5, 1.4, 2H), 4.76 (dt, J = 5.6, 1.4, 4H).

2.3. *RBC-4T1 hybrid membrane preparation*

After low-speed centrifugation (800 rpm, Eppendorf, 5418R, Germany) and PBS (pH 7.4) washing, the obtained RBCs were lysed on ice with 0.25 × PBS (pH 7.4). Then, RBC membrane was collected by high-speed centrifugation (12,000 rpm, Eppendorf). Finally, the sonicated RBC membrane was filtered sequentially with 0.45 and 0.2 μm filters. 4T1 cell membranes were prepared using membrane protein extraction kit (Beyotime, P0033). After determining the protein concentration, the two kinds of membrane were mixed with a ratio of 1:1 and sonicated for 15 min on the ice (50 W, 0.5 s/1 s a cycle), followed water bath stirring at 37 °C for 2 h and extrusion through 0.45 and 0.22 μm filters to obtain RBC-4T1 hybrid membrane.

2.4. *Synthesis of HMPOC@M*

$K_3[Fe(CN)_6]\cdot 3H_2O$ (16 mg) and PVP (2 g) dissolved in the 40 mL HCl (0.01 mol/L) were stirred for 20 h at 80 °C. After centrifugation (12,000 rpm, Eppendorf) and washing, the acquired PB NPs (20 mg) were mixed with PVP (100 mg) in the HCl solution and placed in a reaction vessel at 80 °C for 6 h. The HMPB NPs was collected after water washing. MnCO (5 mg) and HMPB (5 mg) were dissolved in the methanol (10 mL). Then, the mixture was stirred in the dark for 6 h. Finally, the HMPB@CO (HMPO) NPs were collected by centrifugation (12,000 rpm, Eppendorf) and washing with methanol. The methanol mixture containing HMPO NPs (10 mg) and CBD (5 mg) was stirred for 30 min at 50 °C. Then, 80 μg GS-01 was added to the above solution. After stirring for 2 h, distilled water was slowly added. The product was centrifuged (12,000 rpm, Eppendorf) and washed to obtain HMPB@CO@CBD (HMPOC) NPs. For membrane coating, the hybrid membrane and HMPOC were mixed at a weight ratio of 1:2, respectively. After ultrasound on the ice and subsequent extrusion, HMPB@CO@CBD@M (HMPOC@M) NPs were collected by centrifugation.

2.5. *The effects of biomembrane on HMPOC@M behaviors*

Membrane protein characterization: Briefly, total protein concentrations of m4T1, mRBC, 4T1&RBC M or HMPOC@M were detected by the BCA kits. After that, all mixture of samples and loading buffer were heated at 95 °C for 10 min. The levels of CD44 and CD47 in samples were detected using western blot.

Hemolysis assay: RBCs suspension (4% in PBS, *v*/*v*) was incubated with water, PBS, CBD, HMPO, HMPOC and HMPOC@M for 6 h. After centrifugation at 3000 rpm (Eppendorf), the absorbance of the supernatant at 562 nm was used to calculate hemolysis rate. The morphology of RBCs was investigated under microscope (OLYMPUS, IX-73, Japan).

Platelet aggregation assay: Briefly, the platelet-rich plasma from whole blood was first mixed with thrombin (9:1, *v*/*v*), PBS, CBD, HMPO, HMPOC or HMPOC@M (200 μg/mL). Then, the mixtures were incubated at 37 °C for 2 h. After that, the absorbance values of the supernatants at 650 nm were measured for evaluating the turbidity.

Immunogenicity of HMPOC@M *in vivo*: 15 female Balb/c mice were randomly separated into 3 groups and administered with saline, HMPOC, and HMPOC@M, respectively, *via* intravenous injection (0.5 mg/kg PB). LPS (0.5 mg/kg) treated mice *via* intraperitoneal injection were used as the positive control. Then, blood samples were collected from the retro-orbital plexus of mice at 48 h, and centrifuged (3000 rpm, Eppendorf) to obtain plasma for TNF-α and IL-12 assay using ELISA kits.

Cell uptake assay: 4T1 cells in a 24-well plate were treated with HMPOC@M^{Rhb} (containing 30 μg/mL PB and 10 μmol/L CBD) for 2, 4, 6, and 8 h, respectively. The cell nuclei were stained with DAPI. After pre-treatment of methyl-β-cyclodextrin (caveolae-mediated endocytosis), colchicine (micropinocytosis) and chloroquine (lathrin-dependent endocytosis) for 1 h, 4T1 cells were then incubated with HMPOC@M^{Rhb} (containing 30 μg/mL PB and 10 μmol/L CBD) for 6 h. SMC cells, BGC-823 cells or 4T1 cells in a 12-well plate were treated with HMPOC@M^{Rhb} (containing 30 μg/mL PB and 10 μmol/L CBD) for 6 h, respectively. The nuclei of cells were stained with DAPI. Then, RAW264.7 cells in 12-well plates were incubated with HMPOC^{Rhb} and HMPOC@M^{Rhb} (containing 30 μg/mL PB and 10 μmol/L CBD) for 6 h. The nuclei were stained with Hoechst 33342. The intensity difference of red fluorescence emitted by Rhodamine B was investigated under CLSM (OLYMPUS, FV1200, Japan).

2.6. Drug release and CO/Mn production

Photothermal effect assay: A quartz curvet containing 0.5 mL aqueous dispersion of PBS (pH 7.4) or HMPOC@M (30 μg/mL) NPs were irradiated with 808 nm laser (0.75 W/cm^2, 5 min). Temperature changes and infrared images were obtained using infrared induction camera. To gauge the photothermal effect of HMPOC@M, 500 μL of HMPOC@M solutions with different concentration were irradiated with 808 nm laser (0.75 W/cm^2, 5 min). Meanwhile, the laser with different powers were applied to irradiate HMPOC@M solution (30 μg/mL). In addition, the UV−Vis spectra (Shimadzu, UV-1800, Japan) of samples before and after the test cycles were measured to evaluate the photothermal stability of HMPOC@M.

CBD release behavior assay: Dialysis bag containing HMPOC@M solution were immersed into PBS solution (20 mL, pH 7.4 or pH 6.8), followed with 42 °C water bath (simulate 0.75 W/cm^2 irradiation). The release process of CBD was performed on a rotator with a speed of 1000 rpm. At each set time point, the CBD concentration in the PBS solution was monitored by UV−Vis spectra (Shimadzu) measurement. Meanwhile, the release process with 37 °C water bath was performed as the control.

CO release assay: The standard curve of CO was constructed according to the fluorescent intensity at 513.5 nm (HITACHI, F2500, Japan) of FL-CO-1 at the presence of different MnCO concentrations. To evaluate the effect of 100 μmol/L H_2O_2 on CO release, 1 mg/mL HMPOC@M solution was irradiated by 808 nm laser with 0.75 W/cm^2, and then 10 μmol/L FL-CO-1 and 10 μmol/L $PdCl_2$ were added to the above solutions. At predetermined time points, the fluorescent intensity at 513.5 nm was measured to calculate the amount of CO.

Intracellular CO detection: Cells in a 12-well culture plate were treated with different NPs. After incubating for 6 h, a mixture of FL-CO-1 and $PdCl_2$ (2.5 μmol/L: 2.5 μmol/L) was added into the culture medium, and then the corresponding groups were irradiated with 808 nm irradiation. Finally, the cells were washed 3 times with PBS and the fluorescence was imaged with an inverted microscope (OLYMPUS).

Mn^{2+} release assay: The dialysis bag (MW = 3.5 kD) containing 100 μmol/L H_2O_2 and 1 mg/mL HMPOC@M solution (5 mL) was immersed in 50 mL PBS buffer (pH 7.4 or pH 6.8) at 37 or 42 °C (mimic laser stimulation). At desirable time points, 1 mL sample was collected and the same volume of fresh buffer was supplemented. The release profile of Mn^{2+} from HMPOC@M was determined using ICP-MS analysis (Agilent, 8900, USA).

In vitro ·OH generation: Using 5,5-dimethyl-1-pyrroline *N*-oxide (DMPO) as trapping agent, electron paramagnetic resonance spectroscopy was used to detect free radical signal (JEOL, JES-FA 200, Japan). In brief, 25 mmol/L $NaHCO_3/H_2CO_3$ buffer with HMPOC@M (200 μg/mL) was shaken at 37 or 42 °C for 12 h before adding H_2O_2 (final concentration of 1 mmol/L) and DMPO (final concentration of 20 mmol/L). After reaction for 20 min, the EPR spectra of samples were collected on the spectrometer.

Intracellular ·OH detection: 4T1 cells in a 12-well plate were incubated with different NPs for 6 h. After that, the cells were treated with or without irradiation (808 nm, 0.75 W/cm^2, 5 min). Then, APF (10 μmol/L, 5 μL) was added into the culture medium for 30 min. After washing with PBS, images were captured under confocal laser scanning microscope (OLYMPUS).

2.7. Cell lines

4T1 cells, HUVECs, SMC cells and RAW264.7 cells were obtained from the Xiangya Central Laboratory, Central-South University. The cells were cultured in the DMEM medium supplemented with 10% FBS and 1% PS (Invitrogen, Carlsbad, CA, USA).

2.8. In vitro therapeutic effect

SMC cells and HUVEC cells were inoculated into 96-well plates and grown for 24 h. After that, all cells were incubated with HMPB@M (0, 12.5, 25, 50, and 100 μg/mL) for 24 h. Finally, the cytotoxic effect was detected by MTT method.

Before verifying the cytotoxicity of HMPOC@M, the power density of NIR was optimized. In short, 4T1 cells seeded in 96-well plates were incubated with culture medium containing 30 μg/mL HMPB@M. After incubating for 6 h, cells were treated with 808 nm laser. After incubating for another 24 h. MTT method was adopted to evaluate the cytotoxic effect of laser power.

To detect the cytotoxicity of HMPOC@M, 4T1 cells (10,000 per well) seeded in 96-well plates were cultured overnight at 37 °C under 5% CO_2. Then, the cells were treated with different NPs (30 μg/mL PB; 10 μmol/L CBD), respectively. After incubating for 6 h, 4T1 wells were treated with laser irradiation. After incubating for another 24 h, the cytotoxic effect was detected by MTT method.

Cells in a 12-well culture plate were treated with different NPs. After incubating for 6 h, different wells were treated with 0.75 W/cm^2

irradiation. Another 20 h later, calcein-AM (10 μg/mL) and PI (5 μg/mL) was added to stain cells for 30 min, the fluorescence was detected with an inverted fluorescence microscope (OLYMPUS).

4T1 cells in a 12-well plate were incubated with different NPs for 6 h. After that, the cells were treated with or without irradiation (808 nm, 0.75 W/cm^2, 5 min). Then, DCFH-DA (1 μL) was added into the culture medium for 30 min. Fluorescence images of cells were captured using confocal laser scanning microscope (OLYMPUS).

The variation of mitochondrial membrane potential was detected with the JC-1 kit. 4T1 cells were incubated with different NPs for 6 h, and with laser irradiation for 5 min. JC-1 dye was added into the medium for 30 min. After washing with PBS, the fluorescence images were acquired under an inverted microscope (OLYMPUS).

4T1 cells in a 96-well plate were incubated with fresh medium containing different NPs for 4 h before laser irradiation for 5 min. After culturing for 20 h, the harvested cells were lysed to determine protein concentration, following with intracellular ATP assay using an ATP bioluminescent assay kit.

2.9. The evaluation of autophagy in vitro

Western blot analysis: 4T1 cells in 6-well plates were incubated with different NPs for 6 h, followed with laser irradiation or not. After culturing for another 24 h, cells were lysed in the buffer containing protease inhibitors and clarified by spinning at 14,000 rpm for 10 min at 4 °C. Samples were separated using 12% SDS-PAGE and then transferred to polyvinylidene difluoride (PVDF) membranes before incubating with antibody, then incubating with secondary antibody.

Transient expression of mRFP-GFP-LC3: The adenovirus vector containing the mRFP-GFP-LC3 reporters was purchased from Hanbio (HB-LP2100001). Ad-mRFP-GFP-LC3adenovirus was transfected into 4T1 cells at 37 °C with MOI of 20 for 24 h. The red fluorescent protein mRFP, green fluorescent protein (GFP) and LC3 fusion protein could be highly expressed in the 4T1 cells after infection. After different treatments for 16 h, LC3 spots were recorded by confocal laser scanning microscope (λex of mRFP: 580 nm; λex of GFP: 488 nm, OLYMPUS).

Autophagy image: 4T1 cells were incubated with different NPs for 4 h followed with laser irradiation (0.75 W/cm^2, 5 min) or not. After another 4 h of incubation, 4T1 cells were sequentially fixed with 2.5% glutaraldehyde for and osmium tetroxide for 2 h. After dehydration, the cells were embedded into wax for preparing ultrathin sections. The autolysosomes of cell sections were imaged under TEM (JEOL, JEM-2100Plus, Japan).

AO staining: 4T1 cells were incubated with different NPs for 6 h followed with laser irradiation or not. After culturing with new fresh medium for another 10 h, tumor cells were treated with 1 μL AO for 30 min. Then, the cells were washed with PBS and the red fluorescent dots of cells were monitored using fluorescent microscopy (OLYMPUS).

Lysosomal localization: 4T1 cells were incubated with rhodamine-labeled HMPOC@M NPs for 4, 8, 16 and 20 h. Then, tumor cells were treated with 50 nmol/L Lyso-Tracker Green for 30 min. After that, the fluorescence images of cells were acquired under an inverted microscope (OLYMPUS).

In vitro live/dead assay: 4T1 cells were pre-treated with the culture medium containing RAPA (200 nmol/L), 3-MA (1 μmol/L) or CQ (10 μmol/L) for 4 h. Then, the cells were incubated with different NPs (HMPO@M, HMPO@M+PAPA, HMPO@M+3-MA, HMPOC@M, HMPOC@M+PAPA or HMPOC@M+3-MA) for 6 h with the assistance of laser irradiation. After culturing for 20 h, calcein-AM and PI were added for live/dead cells staining.

2.10. Metastasis suppression in vitro

Would healing assay: the wound in 4T1 cells seeded into 6-well plates was prepared by using sterile 200 μL pipette tip. After starving for 6 h, the cells were incubated with the culture medium containing CBD, HMPO@M and HMPOC@M NPs for 6 h with the assistance of laser irradiation. After 48 h, the cells were photographed using a microscope (OLYMPUS).

Invasion assay: 4T1 cells seeded into 6-well plates were incubated with CBD, HMPO@M and HMPOC@M NPs for 48 h. Then, the cells were seeded in the upper chamber coated with 10 μg/mL of diluted Matrigel® at a density of 1×10^5 cells/well. After 48 h incubation, the migrated cells were fixed with 4% paraformaldehyde and stained with 0.1% crystal violet for imaging with optical microscopy (OLYMPUS).

Endothelial tube formation assay: 4T1 cells in a 6-well plate were treated with CBD, HMPO@M+L and HMPOC@M+L. 24 h post-treatment, the medium was removed and replenished with 2% serum-fresh medium for 24 h to finally get conditioned medium. A 24-well plate was coated with reduced growth factor basement membrane matrix (Gibco, 50 μL per cm^2) and incubated at 37 °C to allow gel solidification. The HUVECs were diluted in conditioned medium at a density of 5×10^4 cells per 500 μL. Tube formation was monitored after 6 h and images were taken using an Olympus inverted microscope.

2.11. The transcriptome high throughput sequencing

Total RNAs of treated group (HMPOC+L, $n = 3$) and control group (PBS, $n = 3$) were extracted with TRIZOL according to the manufacturer's instructions. The RNA extraction, purification, reverse transcription, library construction, and sequencing were performed at Lianchuan Biotechnology Co., Ltd. (Hangzhou, China) using Illumina HiSeq4000 (Illumina, San Diego, CA, USA). The gene expression level was determined by calculating the fragments per kilobase of exon per million mapped reads (FPKM) method, which represented fold change and *P*-value of differentially expressed mRNAs. The data were analyzed online with the Omicstudio Platform.

2.12. Animal experiment method

Balb/c mice (4−5 weeks) were purchased from Hunan SJA Laboratory Animal Co., Ltd. All animal experiments conform to the guiding principles of "Declaration of Helsinki" and have been approved by the Medical Ethics Committee of Hunan University.

2.13. In vivo biodistribution in main organs and pharmacokinetics

ICG-labeled HMPOC NPs were synthesized according to self-assemble process of CBD. ICG-labeled HMPOC, HMPOC@M^{RBC}, HMPOC@M^{4T1} or HMPOC@M (2.5 mg/kg of ICG) were injected *via* tail vein for bio-distribution and tumor targeting efficiency assay. The tumors and major organs were isolated for *ex vivo* imaging (Caliper, Lumina xr, USA) after administration for 48 h. After intravenous administration with

HMPOC, HMPOC@M^{RBC}, HMPOC@M^{4T1} or HMPOC@M, 100 μL whole blood of mice were collected at preset time points for fluorescence imaging and quantification. Additionally, the obtained plasma samples were used for serum fluorescence quantification.

2.14. Antitumor effect of HMPOC@M in vivo

The orthotopic 4T1 breast cancer models were established by injecting 4T1 cells (1×10^7 cells) into the mice. When the tumor volume reached about 100 mm^3, the mice were randomly divided into 4 groups (6 mice/per group), as follows: I: PBS, II: CBD, III: HMPO@M, IV: HMPOC@M (CBD: 5 mg/kg; HMPO@M: 5 mg/kg; HMPOC@M: containing 5 mg/kg PB and 5 mg/kg CBD). After intravenous injection, laser treatments (group III and group IV) were treated with NIR irradiation on the second day (808 nm laser with 0.75 W/cm^2 for 5 min). Meanwhile, healthy mice were used as the normal group. Treatment was stopped at 20th day and only observation and documentation were maintained for the remaining 20 days. The body weight and tumor volume were measured and recorded every day. Moreover, all tumors were collected at the end of experiment and the prepared sections were stained with Ki67, H&E, and TUNEL. Meanwhile, other major organs were harvested for H&E staining and spleens were collected for weighing.

2.15. Immunofluorescence imaging

Briefly, antigen-repaired paraffin sections of tumor tissue were immersed in 0.3% Triton X-100 for 30 min. Then, the sections were sequentially sealed with milk and incubated with antibody (anti-MMP9, anti-VEGF, anti-LC3B, anti-SQSTM1 or anti-BECN1) at 4 °C overnight followed with secondary antibody (1:1000, goat anti-rabbit IgG conjugated to Alexa Fluor 488) incubation for 2 h. Finally, DAPI was used to label nuclei. After washing with PBS for 3 times, the fluorescence images were captured under laser scanning confocal microscope (OLYMPUS).

2.16. Statistical analysis

Error bars in all figures were expressed as the mean ± standard deviation (SD) and repeated at least 3 times. Comparative analysis of the difference between groups was calculated by one-way analysis of variance (ANOVA) with Prism 7.0 (95% confidence interval). A significant difference was set at $^{***}P < 0.001$, $^{**}P < 0.01$, and $^{*}P < 0.05$. Values are displayed in the form of mean ± SD.

3. Results and discussion

3.1. Preparation and characterization of HMPOC@M

The preparation process of HMPOC@M was displayed as Scheme 1. After having prepared hollow mesoporous prussian blue nanoparticles (HMPB NPs) through hydrothermal method[31], the as-prepared HMPB NPs had the average size of ~85 nm and uniform cubic shape with outer shell (Supporting Information Fig. S1A). Then, CO-releasing molecule (MnCO) was physically enveloped into the cavity of HMPB to obtain HMPO NPs. The reduction in the average pore size of HMPO (8.317 nm) also indicated the effective loading of MnCO compared to HMPB (14.418 nm) in Fig. S1B. Subsequently, a lipophilic drug cannabidiol (CBD) was encapsulated on the HMPO surface by self-assembly of alkyl ethers (PPG-13-decyltetradeceth-24, GS-01) with amphiphilic qualities, following with biomembrane camouflage to obtain HMPOC@M NPs. The morphology of the corresponding product was monitored by transmission electron microscopy (TEM). After the deposition of MnCO inside and outside the cavity, the surface of HMPO NPs became rough and spherical with a diameter of ~100 nm (Fig. 1A). CBD was encapsulated in HMPO NPs by the self-assembly solvent evaporation method. After final biomembrane coating, prepared HMPOC@M NPs had a thin film structure on the outer layer with a diameter of ~125 nm (Fig. 1B). The energy-dispersive X-ray spectroscopy (EDS) spectra of HMPO and HMPOC@M exhibited uniform distributions of C, N, O, Fe, and Mn (Fig. 1C), in which the presence of CBD and amphiphilic molecules contributed to the elevated levels of elemental C and O. Meanwhile, the mapping image of P as a constituting element of the phospholipid bilayer demonstrated successful biomembrane camouflage. In addition, the ζ-potentials of HMPB and HMPOC@M NPs solution were −16.2 and −22.3 mV, respectively (Fig. 1D), due to the negative charge of CBD and biomembrane[31,32]. UV−Vis spectra show characteristic absorption peaks of CBD and biomembrane at 280 and 410 nm, respectively (Fig. 1E). The fluorescence imaging indicated the independence of red and green fluorescence in the mixed membrane sample, while yellow fluorescence signal was observed in the sample of membrane fusion (Fig. 1F). By performing FRET assay according to our previous method[31], we found that the contrary change of two emission peaks with the amount increase of RBC membrane and successful membrane fusion (Fig. 1G). The characteristic proteins of CD44 and CD47 from two cell membranes were inherited by 4T1&RBC membranes and HMPOC@M (Fig. 1H).

3.2. Biocompatibility and biodistribution assay of HMPOC@M NPs

It was reported that biomembrane camouflage can avoid thrombosis or hemolysis caused by bare NPs during blood circulation[33]. Likewise, we found the ultra-low hemolysis rates (5%) of HMPOC@M with different concentrations in this study, accompanying the complete morphology of erythrocytes (Supporting Information Fig. S2A). Meanwhile, HMPOC@M did not cause platelet aggregation in the blood at all (Fig. S2B). Also, hematological analysis indicated negligible effect of several key indicators (RBC, WBC, HGB, PLT and MPV) in each group (Fig. S2C), compared with the normal group. Importantly, negligible effect was found for HMPOC@M on the TNF-α and IL-12 secretion (Fig. S2D), implying no allergic reaction.

Excellent nano-delivery systems should possess good biocompatibility and tumor-specific targeting so as to ensure drug efficacy. The “don’t eat me” protein (CD47) on the surface of biomembrane allows nanocomplexes to evade the surveillance of the immune system[34]. The adhesion molecule (CD44), a another surface marker, is involved into the adherence of homologous cancer cells[35,36]. Considering the co-existence of CD44 and CD47 in the hybrid membrane, we suspect that HMPOC@M can evade immune surveillance. As shown in Supporting Information Fig. S3A, the uptake efficiency of HMPOC@M decreased significantly compared to bare HMPOC in macrophages. Moreover, the circulation half-life for HMPOC@M was investigated to be 6.62 h, which was longer than that of bare HMPOC or HMPOC@M^{4T1} (2.34 or 4.14 h), while comparable to that of

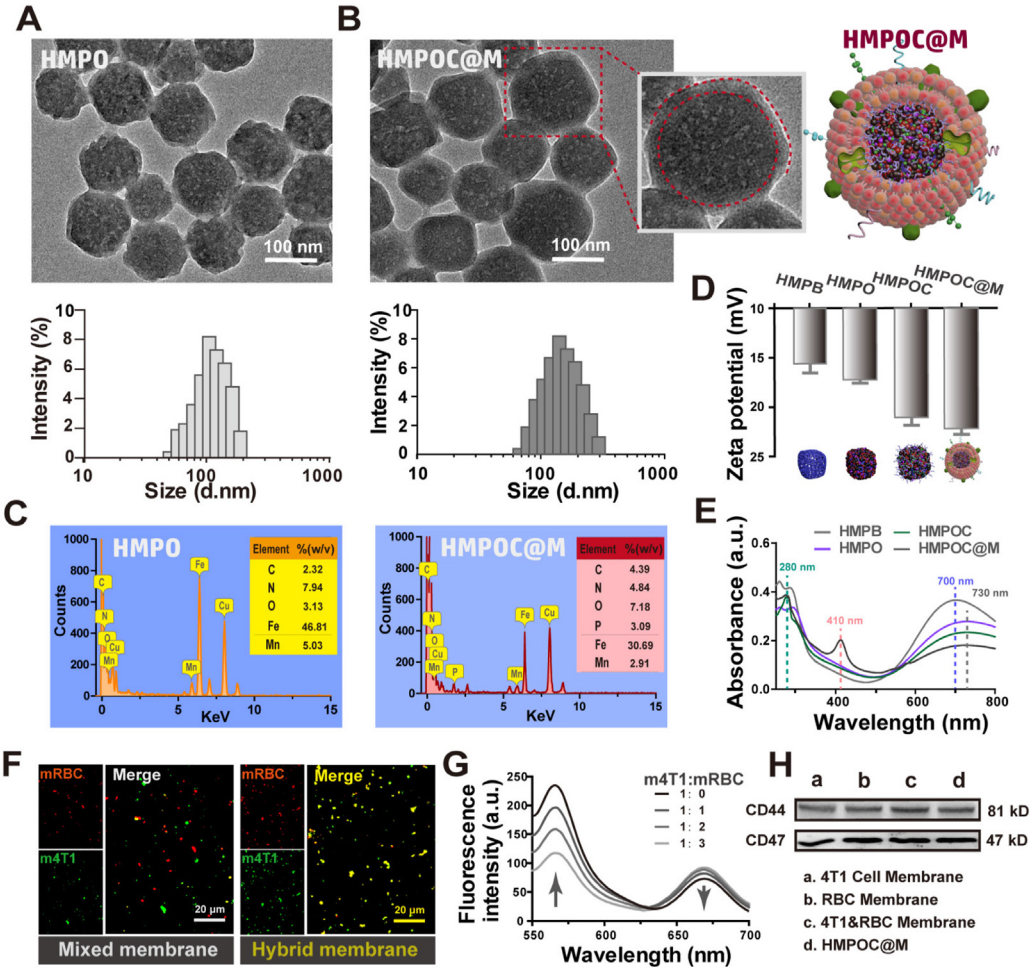

Figure 1 Preparation and characterization of HMPOC@M NPs. (A) TEM images and the particle size distribution of HMPO NPs. (B) TEM images and the particle size distribution of HMPOC@M NPs. (C) EDS spectra on the main element contents of HMPO NPs and HMPOC@M NPs. (D) ζ-Potential measurement of different NPs. Data are presented as mean ± SD, $n = 3$. (E) UV−Vis absorption spectra of NPs. (F) CLSM images of membrane mixture and hybrid membrane. (Red color represents mRBC and green represents m4T1). (G) m4T1 doped with DiO and DiI were mixed with increasing number of mRBC; The recovery of fluorescence signal at 670 nm was recorded. (H) Western blot assay of CD44 (81 kD) and CD47 (47 kD) in different membrane samples.

HMPOC@M^{RBC} (6.85 h, Fig. S3B). This result suggests that RBC membrane can extend the circulation half-life of NPs due to their immune escape ability[37]. Since the targeting ability of NPs was an important prerequisite for effective tumor elimination, we then investigated the uptake behavior of 4T1 cells on HMPOC@M NPs *in vitro*. As shown in Fig. S3C, the uptake efficiency of HMPOC@M showed a time-dependent manner with the saturate signal at 6 h. To further investigate the uptake mechanism, 4T1 cells were pretreated with small molecule endocytosis inhibitors before incubating with HMPOC@M NPs. Significantly, colchicine pretreatment reduced the uptake of HMPOC@M by more than 50% (Fig. S3D), suggesting that most HMPOC@M NPs entered 4T1 cells *via* micropinocytosis. Importantly, the phagocytosis of HMPOC@M by 4T1 cells was significantly higher than that of the other two non-homologous cells (over 2.5-fold, Fig. S3E). Then, we further observed the biodistribution of HMPOC@M *in vivo* by injecting fluorescent-labeled NPs coated with different biomembrane into mice *via* tail vein for 48 h. Fig. S3F indicated that the accumulation of HMPOC@M or HMPOC@M^{4T1} was significantly higher than that of other NPs in tumor, due to the homing effect of 4T1 cell membrane[37]. Quantitative assay indicated that the accumulation of HMPOC@M in the tumor region increased 7.6-fold after coating with hybrid membrane. The enrichment of NPs in the lung, an organ for nanomaterials deposition was observed, which is consistent with previous reports[38].

3.3. *Drug release and CO/Mn^{2+} production*

To determine the drug-carrying capacity of the NPs, drug loading and encapsulation efficiency were assessed by UV spectrometry. Loading rates of MnCO and CBD in HMPOC NPs were about 53.2 ± 3.23% (Supporting Information Fig. S4A), and 11.22 ± 1.12%, respectively (Fig. S4B). Moreover, the hydrodynamic size of HMPOC@M NPs with the polydispersity index (PDI) of less than 0.2 showed negligible change after incubating serum-containing buffer for 3 days (Fig. S4C). This result demonstrated that biomembrane could enhance the stability of the

nano-delivery system by reducing the adsorption of naked HMPOC NPs to serum proteins and avoiding the formation of protein corona[39]. Next, we monitored the temperature change under 0.75 W/cm^2 laser irradiation and found that the temperature of HMPOC@M solution dramatically increased (30 μg/mL, 10 °C) (Supporting Information Fig. S5A). The photothermal conversion efficiency (PCE) of HMPOC@M was calculated to be 35.9% (Fig. S5B) with concentration and laser power-dependent manners (Fig. S5C). Finally, the UV−Vis spectra were not affected after through 6 on/off irradiation cycles (Fig. S5D), implying the good photostability of HMPOC@M. These results provide considerable potential to accurately control drug release in tumor tissue and protect normal cells from thermal damage[40].

Meanwhile, we investigated the effect of pH value and the laser on the CBD release profile of HMPOC@M by UV−Vis assay. Fig. 2A demonstrates that laser irradiation accelerated the leakage of CBD and a burst release of CBD (72%) at acidic condition within 48 h, which can attribute to enhanced hydrogen bonding of amphiphilic alkyl ethers to water in an acidic environment and to the accelerated diffusion of drug molecules by photothermal heating. Next, we synthesized FL-CO-1 probe (Supporting Information Fig. S6) according to the previous method for CO detection[30]. Using H_2O_2 as substrate, we monitored the fluorescence intensity of different samples as previous reported method[30]. As shown in Fig. 2B, the amount of CO generation dramatically elevated to 40 μmol/L within 30 h in the presence of 100 μmol/L H_2O_2 (present at concentrations ranging from 100 μmol/L to 1 mmol/L in tumor)[41]. Furthermore, we detected the production of intracellular CO and found distinct green fluorescence in HMPO@M+L or HMPOC@M+L group (Fig. 2C). Next, ICP-MS assay was used to detect the Mn^{2+} generation and found it was affected by the H_2O_2, laser irradiation and the pH value (Fig. 2D). Then, electron spin resonance (ESR) assay indicated that the strongest peak standing for ·OH appeared in the HMPOC@M + H_2O_2 + HCO_3^- + NIR group. In contrast, no obvious peak was detected in the NPs or H_2O_2 solution (Fig. 2E). Then, aminophenol fluorescein (APF) probe was used to visually illustrate the levels of ·OH in tumor cells as the interaction between ·OH and APF probe can emit green fluorescence. As we expected that the HMPOC@M+L-treated 4T1 cells showed the strongest green fluorescence signal (Fig. 2F) due to the most efficient Mn^{2+} generation and accelerated subsequent ·OH production under acidic environment (Fig. 2G).

3.4. *Cytotoxicity induced by HMPOC@M*

Previous studies have indicated the function of CBD on the regulation of ROS and autophagy[25]. In this study, we also found the concentration-dependent inhibition of CBD on the levels of NRF2 and LAMP1, accompanied by the c-Jun N-terminal kinase (JNK) and BECN1 upregulation (Fig. 3A). This suggests that CBD could amplify oxidative stress and stimulate autophagy in 4T1 cells. Then, we investigated the synergistic effect of HMPOC@M on the cytotoxicity of 4T1 cells *in vitro*. Supporting Information Fig. S7A demonstrated the IC_{50} of CBD alone was 9 μmol/L and the toxicity of HMPB to 4T1 cells and normal cells was negligible (Fig. S7B and C). Meanwhile, viability of cells with HMPO@M +L (30 μg/mL, 0.75 W/cm^2) treatment was 62%, due to the contribution of CO/Mn^{2+} (Fig. 3B). However, the viability was less than 15% after with HMPOC@M+L (Fig. 3B), due to the synergistic effect of CBD and CO/Mn^{2+}. Also, HMPOC@M+L treatment induced the overwhelming cell death in the live/dead staining assay (Fig. 3C), as reflected by the loss of green fluorescence (live cells) in the visual field. This result also supports the synergistic effect of HMPOC@M+L on the cell viability.

CO can induce mitochondrial collapse through generating ROS[4]. As DCFH-DA can be oxidized by ROS to DCF after deacetylation, accompanied by the green fluorescence increase, this probe was used to detect intracellular ROS level caused by CO. As we expected, the HMPO@M+L group presented a moderate green fluorescent signal. However, the HMPOC@M+L group exhibited synergistic effect (amplification of oxidative stress) after introducing CBD (Fig. 3D), which was reflected by the stronger green fluorescence in 4T1 cells. In addition, western blot assay indicated that the levels of NRF2 in 4T1 cells decreased more than 40% after with HMPOC@M+L treatment due to the existence of CBD, while no similar effect was found in tumor cells with HMPO@M+L treatment (Fig. 3H). Considering that NRF2 can cause ROS detoxification in cancer cells[42], this result suggests that NRF2 downregulation could amplify oxidative stress by co-operating with CO/Mn^{2+}. It is well known that the decrease of mitochondrial membrane potential is the important sign of mitochondrial damage[9], JC-1 probe, which can exhibit brighter red fluorescence signal compared to mitochondria with lower membrane potential, was used to detect the effect of ROS on the mitochondrial damage. As shown in Fig. 3E, the red fluorescence in 4T1 cells was wholly replaced by the bright green signal after with HMPOC@M+L treatment. This result demonstrates the strongest damage of HMPOC@M+L treatment on the mitochondria, comparing with other groups. Meanwhile, the swelling of inner mitochondrial cristae gaps and cristae vesicles visually demonstrated the strong mitochondria damage in the 4T1 cell (Fig. 3F). Similarly, the levels of intracellular ATP decreased more than 80% in 4T1 cells after with HMPOC@M+L treatment (Fig. 3G). In addition, western blot assay indicated that p-AMPK/AMPK ratio, responding to intracellular decrease of ATP, was elevated 2.8-fold in 4T1 cells HMPOC@M+L treatment (Fig. 3H). These results comprehensively indicate the strongest damage in 4T1 cells with HMPOC@M+L treatment, which may result in the occurrence of excessive autophagy in 4T1 cells.

3.5. *Mechanisms of autophagy in HMPOC@M therapy*

By observing the autophagy under bio-transmission electron microscopy, we found a lot of autolysosome accumulation (indicated by red arrows) in the 4T1 cells with HMPOC@M+L treatment, demonstrated that HMPOC@M+L and HMPO@M+L treatments could evoke autophagy in 4T1 cells (Fig. 4A). As a molecular sensor for damaged mitochondria, PTEN-induced kinase 1 (PINK1) can trigger the signal of mitophagy initiation and recruit the “enhancer” of PARKIN to mitochondria to amplify the mitophagy signals[43]. Western blot assay indicated the similar upregulation of HMPOC@M+L and HMPO@M+L on the PINK1 and PARKIN levels of tumor cells. The above results demonstrate that HMPOC@M+L can induce mitophagy through PINK1/PARKIN signal pathway (Fig. 4B). It was reported that CBD induced JNK activation can inhibit the interaction between BECN1 and BCL-2 in TNBC[27]. Then, the formed class III PI3K/BECN1 complexes initiate autophagy for cell death[28]. Consistent with previous report[25], we found that CBD can upregulate JNK and BECN1 expression in a concentration-dependent manner (Fig. 3A). Similarly, CBD-contained HMPOC@M+L group

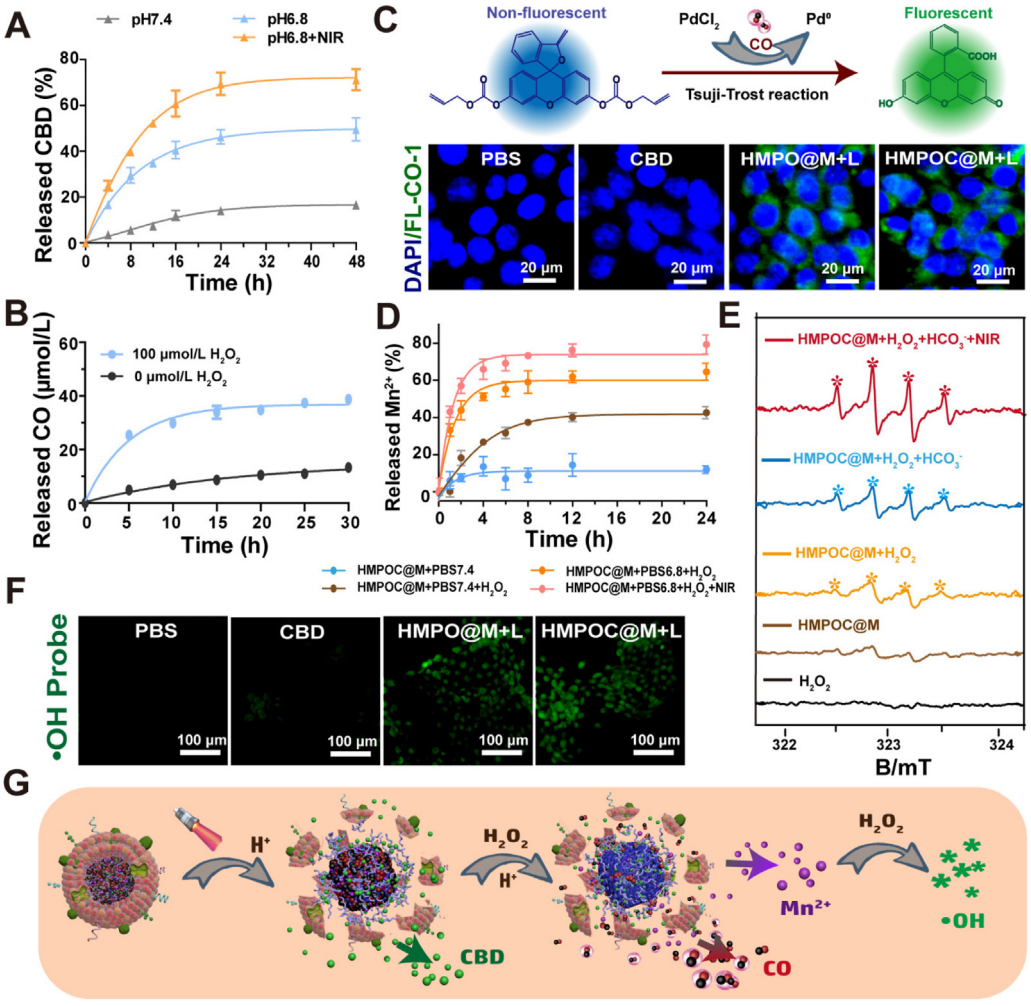

Figure 2 Drug release and CO/Mn^{2+} induced by HMPOC@M. (A) Cumulative release of CBD from HMPOC@M at various simulating conditions. (B) Quantification analysis of CO released from HMPOC@M at the presence of H_2O_2. (C) CLSM images of 4T1 cells treated with PBS, CBD, HMPO@M+L and HMPOC@M+L (0.75 W/cm^2, 5 min). The green channel represented CO release using a CO probe (FL-CO-1). (D) Quantification analysis of Mn^{2+} production from HMPOC@M upon different conditions (100 μmol/L H_2O_2). (E) ESR spectra of samples upon different conditions. (F) CLSM images of 4T1 cells staining with APF. (G) Schematic diagram of drug release and CO/Mn production from HMPOC@M. Data are shown as mean ± SD, $n = 3$.

upregulated BECN1 about 1.5-fold. In addition, both of LC3B (classical initiation proteins of autophagy) and LC3B/LC3A ratio in the HMPOC@M+L treated cells were higher than those of HMPO@M+L-treated cells. These results demonstrate that HMPOC@M+L treatment efficiently induces autophagy through JNK/BECN1 signaling pathway.

Next, we assessed the effect of HMPOC@M+L on the entire process of autophagy. AO staining was first performed to investigate the effect of HMPOC@M+L on late autophagic vesicles (autolysosomes) as the entering of AO into autolysosomes can emit red fluorescence[44]. As shown in Fig. 4C, the red fluorescence signal in the HMPOC@M+L-treated cells significantly decreased comparing with that of HMPO@M+L-treated cells. This result demonstrate that CBD-contained HMPOC@M strongly inhibits the formation of autolysosomes, which can result in the accumulation of autophagosomes (the elevated LC3B levels). The above result in Fig. 3A indicates the inhibiting function of CBD on the LAMP1, a key protein for regulating pH value of lysosomes. We then investigated the effect of HMPOC@M+L on the pH value of lysosomes using Lyso-tracker probe (green fluorescence probe). Fig. 4D demonstrates the gradual decrease of green fluorescence signal in treated cells with the time elongation. Meanwhile, the level of LAMP1 was significantly decreased in 4T1 cells with HMPOC@M treatment (Fig. 4F). These results directly reflected the HMPOC@M can inhibit the formation of autolysosomes through lysosomes alkalization[45]. The mRFP-GFP-LC3 adenovirus transfection was further used to track the autophagy flux in 4T1 cells. Fig. 4E indicates obvious increase of yellow dots in the HMPOC@M+L-treated cells. In contrast, only red dot number increased in the HMPO@M+L-treated cells with same treatment. As yellow dots (the overlapping of red and green fluorescence) and red dots (the quenching of green fluorescence as the acidic environment) represent autophagosomes and autolysosomes[44], respectively, this result also demonstrate that HMPOC@M+L treatment could inhibit autophagy flux by blocking autolysosome formation. Similarly, SQSTM1 upregulation in the HMPOC@M+L-treated cells also reflected the inhibition of autolysosome formation[44]. In contrast, this protein was

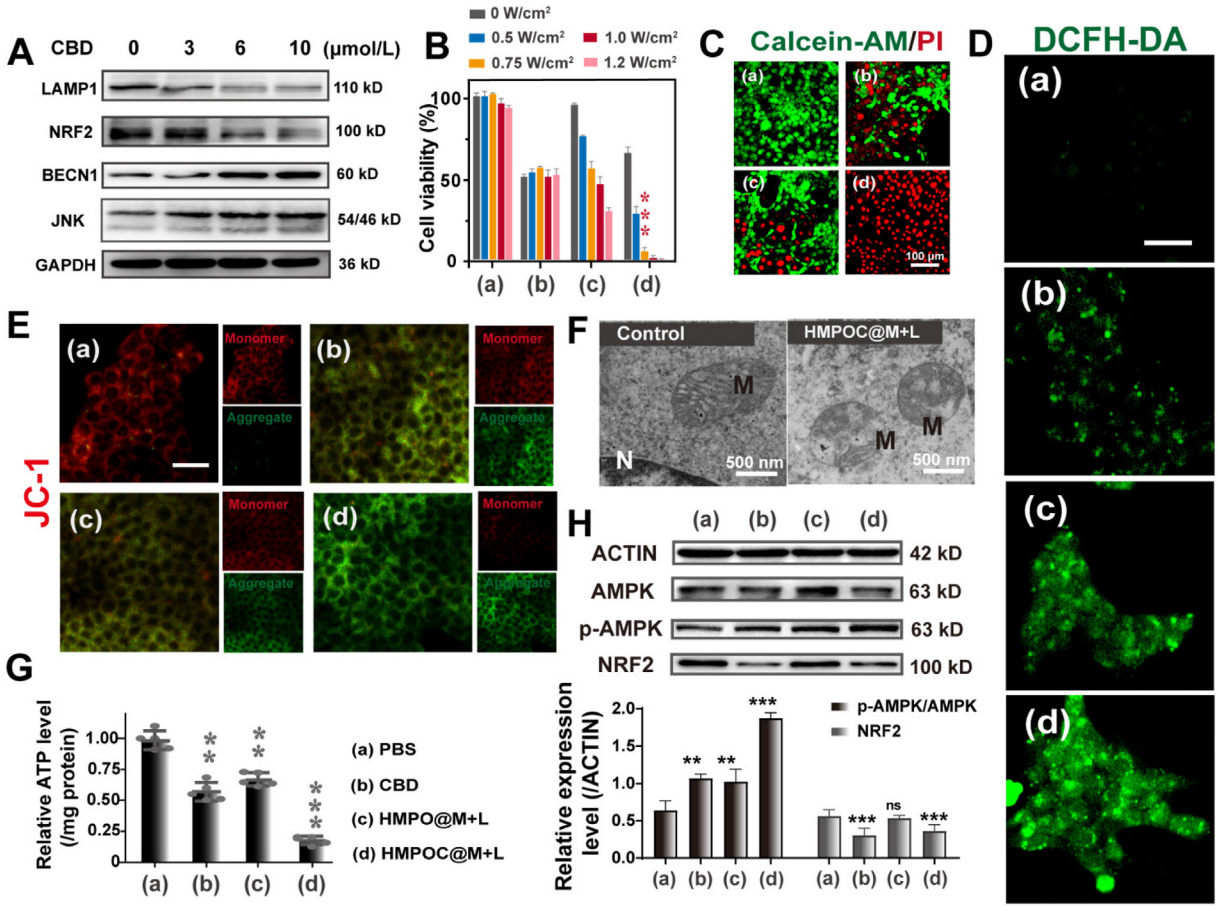

Figure 3 Cytotoxicity induced by HMPOC@M. a: PBS; b: CBD (10 μmol/L); c: HMPO@M+L (30 μg/mL); d: HMPOC@M+L (30 μg/mL). (A) Western blot and quantitative analysis of 4T1 cells treated with different concentration CBD for 24 h. (B) The cell viability of 4T1 cells after incubation with CBD, HMPO@M and HMPOC@M under irradiation. (C) Fluorescence image of 4T1 cells with live-dead staining. (D) CLSM images of DCFH-DA staining in 4T1 cells. (E) CLSM images of 4T1 cells stained by JC-1. (F) Bio-TEM images after 4T1 cells treated with different samples for 8 h. (G) Intracellular ATP level assay per mg of protein in 4T1 cells with different treatment. (H) Western blot and quantitative analysis of AMPK (63kD), p-AMPK (63kD) and NRF2 (100kD) levels in 4T1 cells. Scale bar: 50 μm. Data are shown as mean ± SD, $n = 3$. ANOVA was used to assess statistical significance. $^{**}P < 0.01$, $^{***}P < 0.001$. ns, not significant.

degraded in the HMPO@M+L group (Fig. 4F), due to the normal fusion of autophagosomes and lysosomes[44]. In summary, HMPOC@M+L-induced excessive autophagy was contributed to the accumulation of autophagosomes and the blockade of autolysosome formation.

Next, autophagy regulators (activator and inhibitors) were adopted to confirm the excessive autophagy induced by HMPOC@M+L could efficiently kill tumor cells. According to the result of Supporting Information Fig. S8, we determined the safe concentrations of 1 and 10 μmol/L for 3-MA (early autophagy inhibitor) and CQ (late autophagy inhibitor) without cytotoxicity on tumor cells. However, the presence of 3-MA and CQ with safe concentration increased viability of 4T1 cells with HMPOC@M+L treatment (Fig. 4G). In contrary, the presence of 200 nmol/L RAPA (early autophagy activator) further reduced the viability of 4T1 cells with HMPOC@M+L treatment. This data suggested that mitophagy induced CO/Mn^{2+} can facilitate cancer cell survival. These results, which were consistent with live/dead cell assay (Supporting Information Fig. S9), suggested that the high 4T1 cell killing ability efficiency of HMPOC@M was tightly related with excessive autophagy (Fig. 4H).

3.6. *Transcriptome high-throughput sequencing analysis*

To further illuminate the underlying mechanism of HMPOC@M against tumor cells, transcriptome sequencing was adopted to investigate the mRNA levels of genes in 4T1 cells. The principal component analysis (PCA) and heat map apparently demonstrated transcriptomics change of 4T1 cells caused by HMPOC@M+LNPs (Fig. 5A and B). The venn diagram indicated exclusive expression of 1302 genes in the treatment group, except 22594 genes with co-expression (Fig. 5C). Based on the screening criteria of FDR < 0.05 and $|\log_2 FC| => 1$, 1938 genes were found to involve in the treatment process of HMPOC@M+L, including upregulation of 625 genes and down-regulation of 1313 genes (Fig. 5D and E).

Subsequently, we performed gene ontology (GO) analysis to investigate the biological function of genes with transcription change and found that integral components of mitochondrion were highly enriched in the GO analysis (Supporting Information Fig. S10). Meanwhile, KEGG pathway enrichment analysis revealed the important role of HMPOC@M+L on the regulation of apoptosis, autophagy, MAPK signal pathway, PI3K-Akt-mTOR

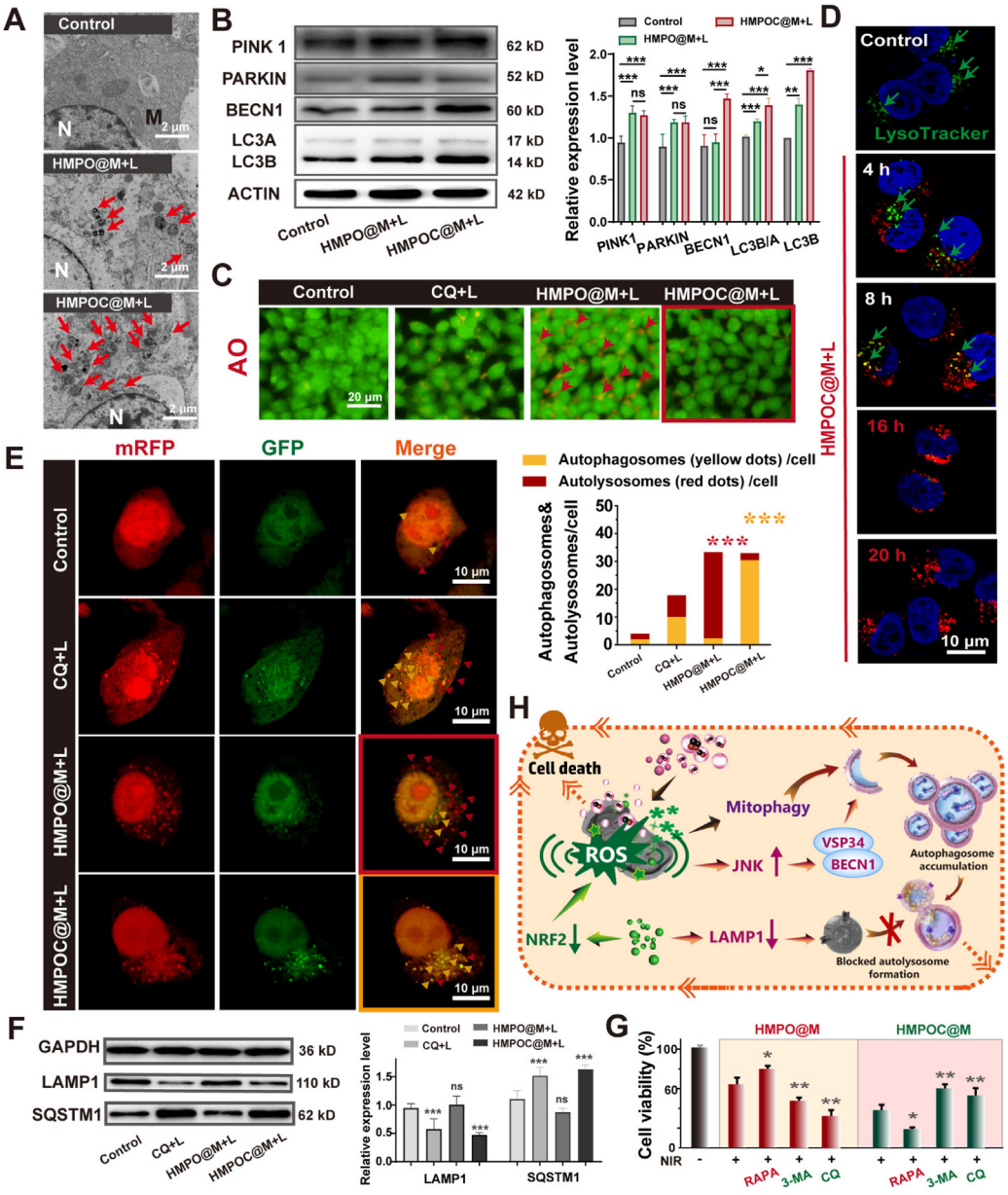

Figure 4 Mechanisms of autophagy in HMPOC@M synergistic therapy. (A) Bio-TEM images after 4T1 cells treated with different samples for 8 h. (B) Western blot and quantitative assay of autophagy-associated proteins in 4T1 cells with different treatment for 24 h. (C) AO-stained fluorescent images in 4T1 cells with different treatments. (D) Confocal fluorescence images of 4T1 cells treated with HMPOC@M (labeled with rhodamine) for different time periods. Before imaging, these cells were stained by Lyso-Tracker Green. (E) Confocal laser scanning microscopy images of 4T1 cells expressing mRFP-GFP-LC3 after different treatments for 16 h (Yellow dots represent autophagosomes and red dots represent autolysosomes) and quantitation of Red LC3 puncta (autolysosome) and yellow LC3B puncta (autophagosome) counted by Image J software. (F) Western blot of LAMP1 (110 kD) and SQSTM1 (62 kD) in cells with different treatment. (G) Cell viability of 4T1 cells after treatment with HMPO@M+L or HMPOC@M+L in the presence of RAPA, 3-MA or CQ. (H) Schematic illustration of excessive autophagy-promoted cell death. Data are shown as mean ± SD, $n = 3$. ANOVA was used to assess statistical significance. *$P < 0.05$, **$P < 0.01$, ***$P < 0.001$. ns, not significant.

signal pathway and p53 signal pathway (Fig. 5F). Moreover, gene set enrichment analysis (GSEA) indicated the significant enrichment of differentially expressed genes in the signal pathways of apoptosis and autophagy (Fig. 5G). It was reported that high ROS level in mitochondria could induce apoptosis by activating the MAPK signal pathway. Meanwhile, the PI3K-Akt-mTOR signal pathway was involved in the cellular autophagy[46,47]. p53 also played an important role in apoptosis and lethal autophagy triggered by mitochondrial dysfunction[48]. By combining with above findings of transcriptome analysis, we can suspect that regulation of autophagic function by HMPOC@M+L NPs is the main reason of efficient TNBC therapy.

Low level of ROS acts as signaling messenger for promoting cancer cell invasion[49]. However, anti-cancer drug-initiated stress

signal could induce excessive ROS to induce cancer cells death. Paradoxically, excessive ROS often induces DNA mutation and/or promotes tumor metastasis at various stages of cancer progression[50]. However, the therapeutics based on ROS is cancer-type and stage-dependent. Considering the high ROS level and autophagy induced by HMPOC@M+L treatment, we investigated its effects on 4T1 cell metastasis. Scratch assay indicated the wound healing rates of tumor cells treated with HMPOC@M+L decreased 62.1%, compared to the control group (Supporting Information Fig. S11A). Transwell invasion assay revealed that both of CBD and HMPOC@M+L treatment significantly attenuated the invasive ability of 4T1 cells compared with the blank control. Quantitative analysis demonstrated the similar invasion rates for CBD- and HMPOC@M+L-treated cells (40.2% *vs.* 38.1%, Fig. S11B). Considering the negligible difference of transwell assay between CBD and HMPOC@M+L treatment, this result directly reflects the inhibitory function of CBD on tumor cell invasion. Western blot assay further demonstrated significant down-regulation of MMP9 and VEGF, the two key proteins of metastasis regulation in CBD- and HMPOC@M+L-treated 4T1 cells. However, no similar effect was found in HMPO@M+L group (Fig. S11C). These data suggest that CBD plays a key role on cancer cell invasion into the extracellular matrix (ECM) by reducing MMP9 secretion[51]. In addition, conditional medium of CBD- or HMPOC@M+L-treated 4T1 cells with low VEGF expression was used to induce endothelial tube formation of HUVECs. By monitoring the number of nodes, number of mesh, and total tube length, we found that all angiogenesis parameters of HUVECs decreased in the conditional medium, comparing with that of whole medium (Fig. S11D). These results suggest that HMPOC@M+L maybe efficiently inhibit distal metastasis of tumor cells by reducing cell infiltration into ECM and blocking angiogenesis.

3.7. *The ablation of HMPOC@M+L on orthotopic 4T1 tumors and anti-metastasis*

The eminent performance of HMPOC@M *in vitro* inspired us to investigate the anti-tumor effect *in vivo*. The schematic illustration of the experimental protocol was shown in Fig. 6A. In this study, 4T1 tumor-bearing mice were randomly divided into four groups including model group (I), CBD group (II), HMPO@M+L group (III), and HMPOC@M+L group (IV). As we expected that HMPOC@M+L treatment significantly inhibited the tumor growth of mice at the end of experiment (Fig. 6B) and some tumors were even ablated during the administration period (Fig. 6C). Quantitative assay indicated that tumor inhibition rate of HMPOC@M+L was significantly higher than that of CBD (95.2% *vs.* 30.2%) and HMPO@M+L (95.2% *vs.* 54.6%) (Fig. 6D). By observing the excessive splenomegaly in the tumor-bearing mice, we found that the spleen weight of mice with HMPOC@M+L administration was close to the normal mice (Fig. 6E), demonstrating the positive immunomodulatory effects of HMPOC@M+L administration[52]. In addition, the survival time of mice with HMPOC@M+L treatment was at least prolonged to 40 days (Fig. 6F), which was longer than the model group (death from 26th day). Meanwhile, the above conclusions were further supported by pathological sections of tumor tissues, including H&E, TUNEL, and Ki67 staining (Fig. 6G). Apparently, the HMPOC@M+L treatment resulted in less proliferation and more apoptosis in tumor tissues. These results further support the *in vivo* antineoplastic therapeutic outcome. Immunofluorescence staining of LC3B, BECN1 and SQSTM1 proteins of tumor tissues was performed to explore the anti-tumor mechanism *in vivo*. The levels of LC3B in HMPOC@M+L group were much higher than that in HMPO@M+L group (Fig. 6H), demonstrating high accumulation

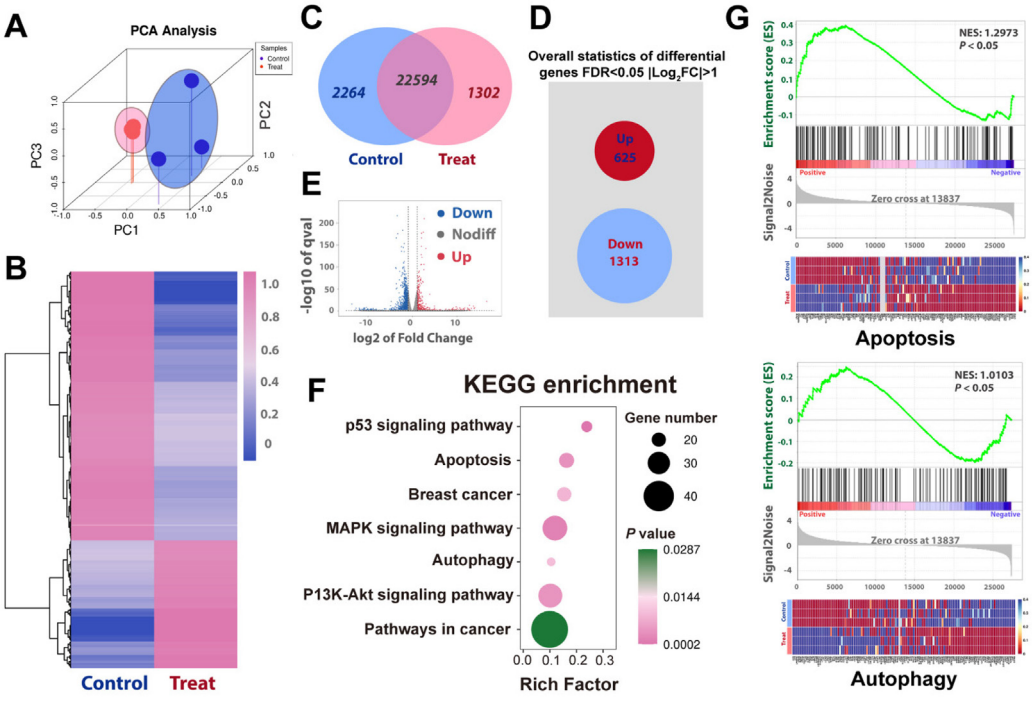

Figure 5 The transcriptome high throughput sequencing assay (n = 3). (A) Principal component analysis (PCA) based on differentially expressed genes. (B) Heat map of differentially expressed mRNAs. (C) Venn diagram of the transcriptomic profiles of cells with HMPOC@M+L treatment or not. (D) Overall statistics of 1938 differential genes, 625 genes with up-regulation, while 1313 genes with down-regulation. (E) The volcano map. (F) Bubble diagram of genes enriched in KEGG pathway. (G) GSEA for apoptosis and autophagy pathway.

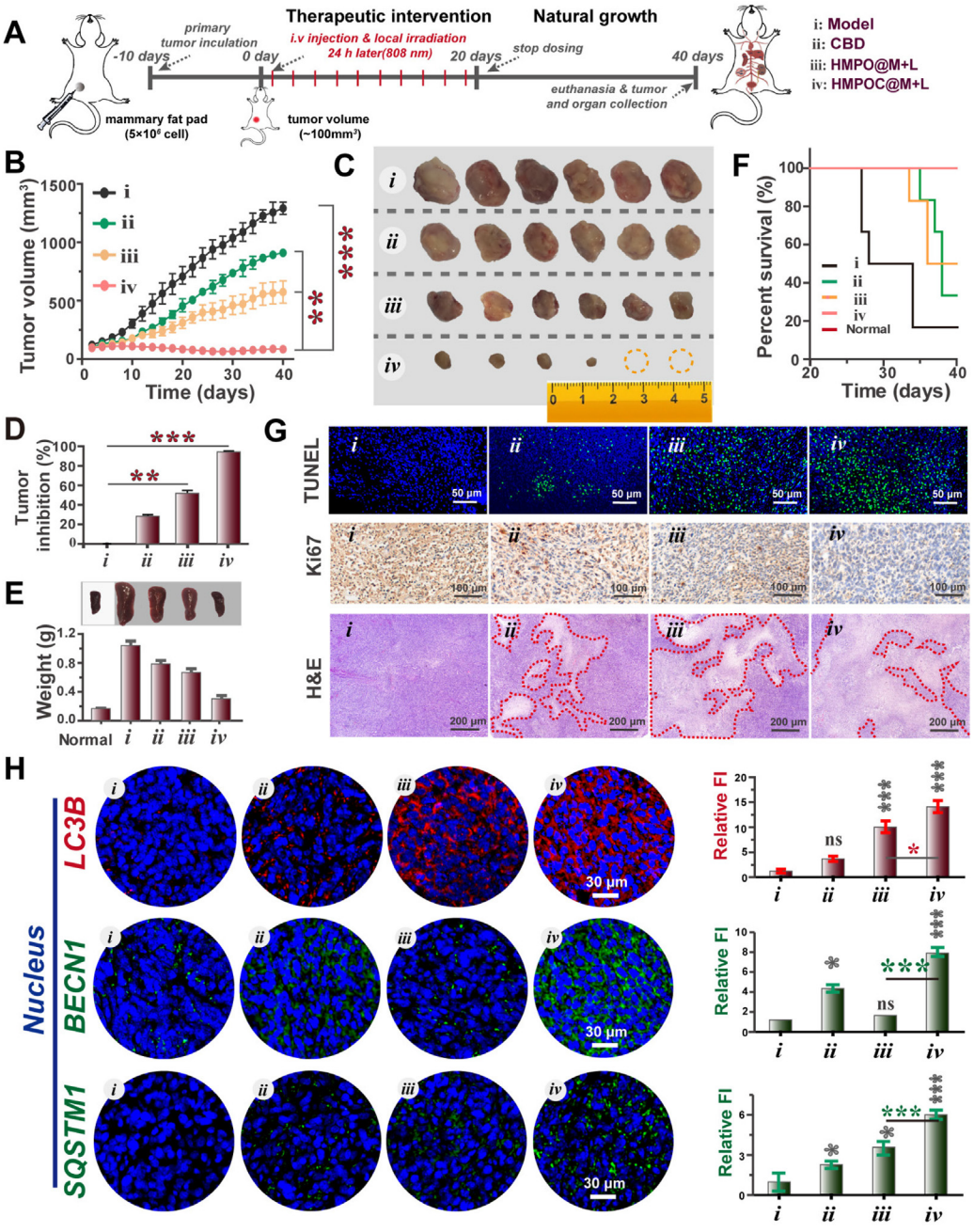

Figure 6 *In vivo* anti-tumor evaluation of HMPOC@M on orthotopic 4T1 tumors. (A) Schematic illustration of 4T1 orthotopic tumor inoculation and dosing regimen (i: model group; ii: CBD group; iii: HMPO@M+L group; iv: HMPOC@M+L group). (B) Tumor volume change curves ($n = 6$). (C) Images of orthotopic tumors harvested from the mice with different treatment. (D) Tumor inhibition of different groups ($n = 6$). (E) Images and weights of spleens of mice with different treatment. (F) The survival rate of mice with different treatment during the 40-d observation period. (G) H&E, TUNEL and Ki67 staining of tumor sections. (H) Images and quantitative analysis of LC3B, BECN1 and SQSTM1 immunofluorescence staining of tumor sections. Data are shown as mean ± SD, $n = 6$. ANOVA was used to assess statistical significance. *$P < 0.05$, **$P < 0.01$, ***$P < 0.001$. ns, not significant.

of autophagosomes in tumor cells. Meanwhile, upregulation of BECN1 in CBD and HMPOC@M+L groups indicated that increased level of autophagy was performed *via* CBD-mediated class III PI3K/BECN1 complex activation. In addition, compared to the Model group, the levels of SQSTM1 in tumor cells increased 6.2-fold after with HMPOC@M+L treatment. This result, which is consistent with the above finding in the cultured cells, suggests that SQSTM1 accumulation can block autolysosome formation. Except for strong anti-tumor growth effect of HMPOC@M+L administration, H&E staining result indicated significant decrease of pulmonary metastatic nodules in the lung and liver of mice (Fig. 7A). In contrast, severe metastases were found in the model and HMPO@M+L group without CBD. To further verify the *in vivo* anti-metastasis mechanism, we executed

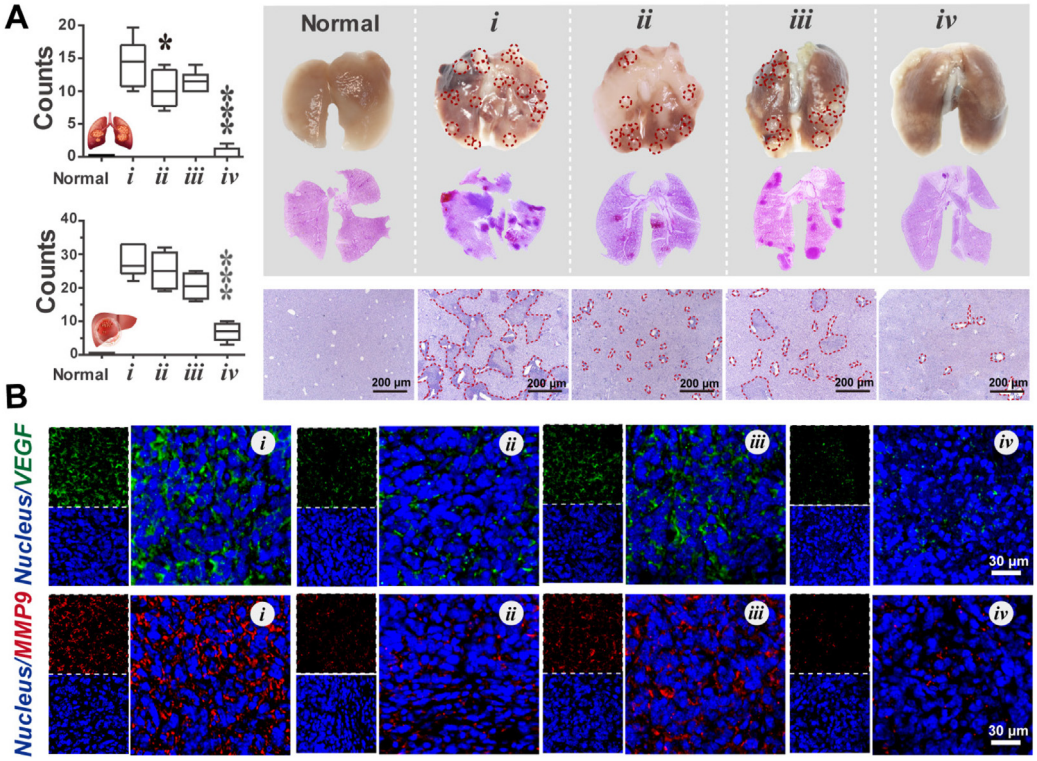

Figure 7 *In vivo* anti-metastasis evaluation (I: model group, II: CBD group, III: HMPO@M+L group, IV: HMPOC@M+L group). (A) Images and H&E sections of lung tissues (the red arrow indicated metastatic nodules) and liver tissues, following with quantitative analysis of metastatic nodules. (B) Images of VEGF and MMP9 immunofluorescence staining of tumor sections. Data are shown as mean ± SD, $n = 3$. ANOVA was used to assess statistical significance. $^{*}P < 0.05$, $^{***}P < 0.001$.

immunofluorescence staining assays of VEGF and MMP9 proteins, the risk factors of breast cancer recurrence and metastasis. Immunofluorescence staining indicated the significant decrease of fluorescent signal intensity in tumor tissues of CBD- or HMPOC@M+L-treated mice, reflecting the inhibitory effect of CBD on the VEGF and MMP9 (Fig. 7B). These data demonstrate that the released CBD from HMPOC@M can effectively suppress lung and liver metastasis of tumor by down-regulating the levels of VEGF and MMP9.

To assess the *in vivo* toxicity, the metabolism and clearance of Mn from HMPOC@M in mice was first investigated by ICP-MS analysis of urine and feces at different times. After 1 day, the content of Mn element in urine and feces was determined to be 20.3% and 4.5% ID/g. As the time was extended to 7 days, the content in urine decreased to 2.5% and 0.7% ID/g (Supporting Information Fig. S12A). The high levels of Mn in urine confirmed that the Mn^{2+} released from HMPOC@M was gradually excreted through the renal pathway. Finally, the pathological and biochemical assay were performed to evaluate the long-term effect of HMPOC@M *in vivo*. No pathological and body weight changes were observed in primary tissue sections of these investigated mice (Fig. S12B and C). There was no significant difference in biochemical function index values between the normal group and the HMPOC@M group (Fig. S12D). However, these results indicated the biosafety of HMPOC@M for anti-tumor application *in vivo*.

4. Conclusions

In this work, a biomimetic cannabidiol synergistic carbon monoxide nanocomplex (HMPOC@M) has been rationally developed for efficient TNBC therapy by comprehensive therapy *via* excessive autophagy. This nanocomplex was confirmed to possess targeted and intelligent delivery into tumors. In addition, we successfully verified that the combination of carbon monoxide and Mn-based Fenton reaction induced mitochondrial dysfunction and mitophagy. In this study, CBD not only amplified oxidative stress by inhibiting NRF2 expression, but also induced excessive autophagy *via* autophagosome accumulation and the blockade of autophagosome formation, which finally resulted in the efficient breast cancer cell death. *In vivo* assay demonstrated the strong inhibitory effect of HMPOC@M on the growth and distance metastasis of TNBC bearing mice by inhibiting metastasis-related proteins. In our points, this comprehensive strategy will open a new door for efficient triple-negative breast cancer therapy through CBD-induced excessive autophagy.

Acknowledgments

This work was partially supported by the Natural Science Foundation of Hunan Province (2020JJ4005; 2020JJ5421; 2021JJ30096, China); National Natural Science Funds of China (82003931); The China Postdoctoral Science Foundation (2021M690974, China); Agricultural Science and Technology Innovation Project of Chinese Academy of Agricultural Sciences (CAAS-ASTIP-IBFC04, China); Opening foundation of Key Laboratory of Study and Discovery of Small Targeted Molecules of Hunan Province (2022CG01, China); Key Research and Development Projects in Ningxia Autonomous Region (2022BFH02013, China).

Author contributions

Chang Xiao prepared the nanopaticles and performed the characterization and cell experiments; Yue Sun, Ying Long, Jialong Fan, William Nguyend and Simin Chen participated in animal experiments; Chang Xiao wrote the manuscript with contributions from Bin Liu, Wei Chen, Aiguo Zhu; Bin Liu provided conceptual advice and revised the manuscript. All the authors contributed to the proofreading and corrections of the manuscript.

Conflicts of interest

The authors have no conflicts of interest to declare.

Appendix A. Supporting information

Supporting data to this article can be found online at https://doi.org/10.1016/j.apsb.2023.05.019.

References

1. Yang GZ, Fan MN, Zhu JW, Ling C, Wu LH, Zhang X, et al. A multifunctional anti-inflammatory drug that can specifically target activated macrophages, massively deplete intracellular H_2O_2, and produce large amounts CO for a highly efficient treatment of osteoarthritis. *Biomaterials* 2020;**255**:120155.
2. Xiao X, Liang S, Zhao YJ, Pang ML, Ma Pa, Cheng ZY, et al. Multifunctional carbon monoxide nanogenerator as immunogenic cell death drugs with enhanced antitumor immunity and antimetastatic effect. *Biomaterials* 2021;**277**:121120.
3. Wu JR, Meng ZY, Exner AA, Cai XJ, Xie X, Hu B, et al. Biodegradable cascade nanocatalysts enable tumor-microenvironment remodeling for controllable CO release and targeted/synergistic cancer nanotherapy. *Biomaterials* 2021;**276**:121001.
4. Zhou Y, Yu WQ, Cao J, Gao HL. Harnessing carbon monoxide-releasing platforms for cancer therapy. *Biomaterials* 2020;**255**:120193.
5. Li JM, Zhou Y, Liu JQ, Yang XT, Zhang K, Lei L, et al. Metal-phenolic networks with ferroptosis to deliver NIR-responsive CO for synergistic therapy. *J Contr Release* 2022;**352**:313−27.
6. Szabo C. Gasotransmitters in cancer: from pathophysiology to experimental therapy. *Nat Rev Drug Disc* 2016;**15**:185−203.
7. Chen L, Zhou SF, Su L, Song J. Gas-mediated cancer bioimaging and therapy. *ACS Nano* 2019;**13**:10887−917.
8. Huang JS, Li YC, Zhang L, Wang J, Xu ZG, Kang YJ, et al. A platinum nanourchin-based multi-enzymatic platform to disrupt mitochondrial function assisted by modulating the intracellular H_2O_2 homeostasis. *Biomaterials* 2022;**286**:121572.
9. Mayevsky A. Mitochondrial function and energy metabolism in cancer cells: past overview and future perspectives. *Mitochondrion* 2009;**9**:165−79.
10. Guo XL, Yang ND, Ji WH, Zhang H, Dong X, Zhou ZQ, et al. Mito-bomb: targeting mitochondria for cancer therapy. *Adv Mater* 2021;**33**:2007778.
11. Amaravadi RK, Kimmelman AC, Debnath J. Targeting autophagy in cancer: recent advances and future directions. *Cancer Discov* 2019;**9**:1167−81.
12. Chakraborty P, Parikh RY, Choi S, Tran D, Gooz M, Hedley ZT, et al. Carbon monoxide activates PERK-regulated autophagy to induce immunometabolic reprogramming and boost antitumor T-cell function. *Cancer Res* 2022;**82**:1969−90.
13. Zhang YJ, Sha R, Zhang L, Zhang WB, Jin PP, Xu WG, et al. Harnessing copper-palladium alloy tetrapod nanoparticle-induced pro-survival autophagy for optimized photothermal therapy of drug-resistant cancer. *Nat Commun* 2018;**9**:4236.
14. Yu W, Wang YT, Zhu J, Jin LB, Liu B, Xia KS, et al. Autophagy inhibitor enhance ZnPc/BSA nanoparticle induced photodynamic therapy by suppressing PD-L1 expression in osteosarcoma immunotherapy. *Biomaterials* 2019;**192**:128−39.
15. Towers CG, Thorburn A. Therapeutic targeting of autophagy. *EBioMedicine* 2016;**14**:15−23.
16. Mukhopadhyay S, Sinha N, Das DN, Panda PK, Naik PP, Bhutia SK. Clinical relevance of autophagic therapy in cancer: investigating the current trends, challenges, and future prospects. *Crit Rev Clin Lab Sci* 2016;**53**:228−52.
17. Tang H, Sebti S, Titone R, Zhou Y, Isidoro C, Ross TS, et al. Decreased *BECN1* mRNA expression in human breast cancer is associated with estrogen receptor-negative subtypes and poor prognosis. *EBioMedicine* 2015;**2**:255−63.
18. Fan MM, Gao J, Zhou L, Xue WW, Wang YX, Chen JW, et al. Highly expressed SERCA2 triggers tumor cell autophagy and is a druggable vulnerability in triple-negative breast cancer. *Acta Pharm Sin B* 2022;**12**:4407−23.
19. Maxfield KE, Macion J, Vankayalapati H, Whitehurst AW. SIK2 restricts autophagic flux to support triple-negative breast cancer survival. *Mol Cell Biol* 2016;**36**:3048−57.
20. Xiang HG, Zhang JF, Lin CC, Zhang L, Liu B, Ouyang L. Targeting autophagy-related protein kinases for potential therapeutic purpose. *Acta Pharm Sin B* 2020;**10**:569−81.
21. Rubinsztein DC, Codogno P, Levine B. Autophagy modulation as a potential therapeutic target for diverse diseases. *Nat Rev Drug Disc* 2012;**11**:709−30.
22. Yang Y, Wang Q, Song DJ, Zen RR, Zhang L, Wang YJ, et al. Lysosomal dysfunction and autophagy blockade contribute to autophagy-related cancer suppressing peptide-induced cytotoxic death of cervical cancer cells through the AMPK/mTOR pathway. *J Exp Clin Cancer Res* 2020;**39**:197.
23. Heider CG, Itenberg SA, Rao J, Ma H, Wu X. Mechanisms of cannabidiol (CBD) in cancer treatment: a review. *Biology* 2022;**11**:817.
24. Pisanti S, Malfitano AM, Ciaglia E, Lamberti A, Ranieri R, Cuomo G, et al. Cannabidiol: state of the art and new challenges for therapeutic applications. *Pharmacol Therapeut* 2017;**175**:133−50.
25. Shrivastava A, Kuzontkoski PM, Groopman JE, Prasad A. Cannabidiol induces programmed cell death in breast cancer cells by coordinating the cross-talk between apoptosis and autophagy. *Mol Cancer Ther* 2011;**10**:1161−72.
26. Ligresti A, Moriello AS, Starowicz K, Matias I, Pisanti S, De Petrocellis L, et al. Antitumor activity of plant cannabinoids with emphasis on the effect of cannabidiol on human breast carcinoma. *J Pharmacol Exp Ther* 2006;**318**:1375.
27. Ivanov VN, Grabham PW, Wu CC, Hei TK. Inhibition of autophagic flux differently modulates cannabidiol-induced death in 2D and 3D glioblastoma cell cultures. *Sci Rep* 2020;**10**:2687.
28. Wei YJ, Sinha S, Levine B. Dual role of JNK1-mediated phosphorylation of BCL-2 in autophagy and apoptosis regulation. *Autophagy* 2008;**4**:949−51.
29. Man SM, Kanneganti TD. Regulation of lysosomal dynamics and autophagy by CTSB/cathepsin B. *Autophagy* 2016;**12**:2504−5.
30. Feng SM, Liu DD, Feng WY, Feng GQ. Allyl Fluorescein ethers as promising fluorescent probes for carbon monoxide imaging in living cells. *Anal Chem* 2017;**89**:3754−60.
31. Xiao C, Tong CY, Fan JL, Wang Z, Xie Q, Long Y, et al. Biomimetic nanoparticles loading with gamabutolin-indomethacin for chemo/-photothermal therapy of cervical cancer and anti-inflammation. *J Contr Release* 2021;**339**:259−73.
32. Zhong GW, Tong CY, Liu X, Fan JL, Xiong X, Chen P, et al. Chi@HMPB@CBD nanocomplexes for laser-assisted therapy of MRSA-infected cutaneous wounds in normal and MKR diabetic mice. *Mater Today Chem* 2022;**24**:100888.
33. Yallapu MM, Ebeling MC, Jaggi M, Chauhan SC. Plasma proteins interaction with curcumin nanoparticles: implications in cancer therapeutics. *Curr Drug Metab* 2013;**14**:504−15.

34. Liu RJ, He L, Liu MY, Chen L, Hou J, Shi JY, et al. Erythrocyte membrane encapsulated gambogic acid nanoparticles as a therapeutic for hepatocellular carcinoma. *Chin Chem Lett* 2023;**34**: 107575.
35. Ren YZ, Jing HQ, Zhou Y, Ren CC, Xiao GX, Wang SY, et al. 4T1 cell membrane-derived biodegradable nanosystem for comprehensive interruption of cancer cell metabolism. *Chin Chem Lett* 2023:108161.
36. Yang R, Xu J, Xu LG, Sun XQ, Chen Q, Zhao YH, et al. Cancer cell membrane-coated adjuvant nanoparticles with mannose modification for effective anticancer vaccination. *ACS Nano* 2018;**12**:5121−9.
37. Liu WL, Zou MZ, Qin SY, Cheng YJ, Ma YH, Sun YX, et al. Recent advances of cell membrane-coated nanomaterials for biomedical applications. *Adv Funct Mater* 2020;**30**:2003559.
38. Wang Z, Long Y, Fan JL, Xiao C, Tong CY, Guo C, et al. Biosafety and biocompatibility assessment of Prussian blue nanoparticles *in vitro* and *in vivo*. *Nanomedicine* 2020;**15**:2655−70.
39. Ke PC, Lin S, Parak WJ, Davis TP, Caruso F. A decade of the protein corona. *ACS Nano* 2017;**11**:11773−6.
40. Wu CS, Wu YH, Zhu XH, Zhang J, Liu JL, Zhang Y. Near-infrared-responsive functional nanomaterials: the first domino of combined tumor therapy. *Nano Today* 2021;**36**:100963.
41. Fu LH, Wan Y, Qi C, He J, Li C, Yang C, et al. Nanocatalytic theranostics with glutathione depletion and enhanced reactive oxygen species generation for efficient cancer therapy. *Adv Mater* 2021;**33**: 2006892.
42. Shen HM, Liu ZG. JNK signaling pathway is a key modulator in cell death mediated by reactive oxygen and nitrogen species. *Free Radical Bio Med* 2006;**40**:928−39.
43. Geisler S, Holmström KM, Skujat D, Fiesel FC, Rothfuss OC, Kahle PJ, et al. PINK1/PARKIN-mediated mitophagy is dependent on VDAC1 and p62/SQSTM1. *Nat Cell Biol* 2010;**12**:119−31.
44. Klionsky DJ, Abdel-Aziz AK, Abdelfatah S, Abdellatif M, Abdoli A, Abel S, et al. Guidelines for the use and interpretation of assays for monitoring autophagy (4th edition). *Autophagy* 2021;**17**:1−382.
45. Busschaert N, Park SH, Baek KH, Choi YP, Park J, Howe EN, et al. A synthetic ion transporter that disrupts autophagy and induces apoptosis by perturbing cellular chloride concentrations. *Nat Chem* 2017;**9**: 667−75.
46. Santarpia L, Lippman SM, El-Naggar AK. Targeting the MAPK−RAS−RAF signaling pathway in cancer therapy. *Expert Opin Ther Targets* 2012;**16**:103−19.
47. Xu ZR, Han X, Ou DM, Liu T, Li ZX, Jiang GM, et al. Targeting PI3K/AKT/mTOR-mediated autophagy for tumor therapy. *Appl Microbiol Biotechnol* 2020;**104**:575−87.
48. Sui XB, Jin LJ, Huang XF, Geng SM, He C, Hu XT. p53 signaling and autophagy in cancer: a revolutionary strategy could be developed for cancer treatment. *Autophagy* 2011;**7**:565−71.
49. Liao Z, Chua D, Tan NS. Reactive oxygen species: a volatile driver of field cancerization and metastasis. *Mol Cancer* 2019;**18**:65.
50. Zhang W, Wang F, Hu C, Zhou Y, Gao HL, Hu J. The progress and perspective of nanoparticle-enabled tumor metastasis treatment. *Acta Pharm Sin B* 2020;**10**:2037−53.
51. Egeblad M, Werb Z. New functions for the matrix metalloproteinases in cancer progression. *Nat Rev Cancer* 2002;**2**:161−74.
52. Marçais A, Walzer T. An immunosuppressive pathway for tumor progression. *Nat Med* 2018;**24**:260−1.